Alexis Nelson

Effects of Stride Length on Knee Loading in Simulated Obese Populations

Faculty Sponsor

Dr. Douglas Powell

Abstract

Walking is part of our daily activities. Increasing body mass potentially increases biomechanical mal-adaptations including reduced step length (SL), and increases joint loading (JRF). The purpose of this study was to determine if acutely added mass (AM) or SL change knee JRFs during walking. Hypotheses included: AM will alter SL, reduced SLs will increase JRFs, and AM increase JRFs. Fourteen participants performed eight trials in four experimental conditions including two variations of SLs, and AM. 3D kinematics and ground reaction forces were collected simultaneously using an 8-camera motion capture system (240 Hz, Qualisys, Inc.) and force platforms (1200 Hz, AMTI, Inc.). Visual 3D was used to calculate joint angles, moments, powers and JRFs. Reduced SL had greater joint flexion angles, peak extension power, and JRFs than AM condition. It was concluded that reduced SLs are associated with greater JRFs while AM in isolation does not alter joint biomechanics.

Introduction

According to the National Institute of Diabetes, 70% of the United States population is overweight or obese ("Key Health Data About Tennessee," 2018). Tennessee itself has the sixth highest rate of obesity in the nation. Further, Memphis had an obesity rate of 33.8% in 2015 (Diseases, 2017; Ruiz, 2012). These statistics reveal that Memphis is one of the most obese cities in America ("Tennessee State Obesity Data, Rates and Trends," 2018). From 1990 to 2015, the obesity rate in Tennessee increased by 20% and continues to increase (Ruiz, 2012). As a nation, the prevalence of obesity is predicted to be 30-37% in men and 34-44% in women by the year of 2020 (Adams et al., 2006). Increasing obesity rates result in secondary increases in cardiovascular and musculoskeletal disorders which result in a concomitant increase in healthcare costs. Obesity-related medical expenses totaled an average of $26 billion dollars per year in the United States from 2005 to 2011. Medical expenses are greater for obese individuals, who are estimated to pay an additional $2,700 to $3,600 per year compared to healthy individuals (Cawley & Meyerhoefer, 2012). As a country, state and city, we are collectively affected by obesity.

Obesity is a scale of excess weight that is associated with adverse health effects (Bessesen, 2008). A widely accepted way to assess excess weight is through a body mass index (BMI). BMI is calculated as the quotient of an individual's body mass divided by their height (in meters) squared (Haff & Triplett, 2016). BMI is used to categorize individuals as underweight (< 18 kg/m2), normal (18 kg/m2 – 25 kg/m2), overweight (25 kg/m2 – 30 kg/m2) or obese (>30 kg/m2). A positive correlation exists between BMI and mortality rates with greater BMI associated with a higher mortality rate (Adams et al., 2006). It is suggested that even modest increases in body weight have negative effects on lifespan (Figure 1), and that the serious negative effects of increasing body weight are not solely due to higher BMI values, but are the result of secondary effects of obesity including metabolic disorders, hyperlipidemia, hypertension, and diabetes (Gregg et al., 2005).

Though obesity has deleterious effects on cardiovascular and metabolic health, obesity is also known to lead to chronic musculoskeletal conditions such as osteoarthritis (Felson, Anderson, Naimark, Walker, & Meenan, 1988; Mohammed, Al-Numair, & Balakrishnan, 2015). Osteoarthritis (OA) is a progressive degenerative disorder of the articular cartilage around a joint: in this case, the knee. Twenty-seven million people in the United States have been diagnosed with OA, equating to more than 8% of the national population ("NIH fact Sheets – Osteoarthritis," 2018). OA accounts for an estimated $10 billion in healthcare costs each year (Bliddal, 2008). Every 5kg

of weight gained increases the risk of osteoarthritis by 36% (Lementowski & Zelicof, 2008). Increasing body mass is associated with greater mechanical loading to the lower extremity. This mechanical loading is created through biomechanical maladaptations such as a reduced step length. Reduced step lengths equate to a greater step width and increased knee joint load.

Obese populations demonstrate aberrant gait biomechanics. Specifically, obese individuals walk with shorter step lengths and greater step widths compared to healthy individuals. A shorter step length is suggested to direct the forces of the system in a vertical direction, which may increase skeletal joint loading (DeVita & Hortobagyi, 2003; Westlake, Milner, Zhang, & Fitzhugh, 2013). A larger step width decreases peak knee joint moments and an increase in mediolateral ground reaction forces, causing abnormal motion and loading in the knee joint, and increasing the risk of musculo-skeletal insult and injury (Yocum, Weinhandl, Fairbrother, & Zhang, 2018). A knee joint moment is the rotational force applied to the joint. These two factors in combination (increased load and greater skeletal involvement) may underlie the higher rates of osteoarthritis in obese individuals exacerbating a sedentary lifestyle and furthering their obesity.

Mechanically, obesity affects multiple aspects of daily living (ADLs). To participate in ADLs, functional capacity has to be present with a low disability. Functional capacity for individuals overall decreases as BMI increases (Adams et al., 2006). Past research has also found a positive correlation between disability and obesity (Alley & Chang, 2007). Specifically, disability in this case will be defined by the increase in knee OA. The pathophysiologic process of knee OA has been identified biomechanically as an increase in knee-joint forces and knee-joint moments. Past research has examined this through changes in body mass (i.e. weight loss). Knee joint adduction moments have been related to an increase in compressive loads (Andriacchi, 1994), and weight loss has been found to reduce significant compressive knee-joint loads, or forces (Milner, Meardon, Hawkins, & Willson, 2018). Overall, obesity impedes movement, hindering the individual's ability to perform basic, daily activities. Many daily tasks require physical activity, which decreases BMI ratings, obesity, and mortality rates (Sui et al., 2007). A daily task that is available and physically demanding to most individuals is walking. A successful treatment many physicians prescribe to increase physical activity is to increase step goals for obese individuals. In order for obese individuals to increase physical activity per day, walking mechanics are important to examine. Doing so ensures that these individuals do not have secondary effects from an increase in walking prescription.

Though it is clear obesity results in altered gait biomechanics, the role of shorter step lengths on knee joint loading in obese individuals has not been established. Messier et al. (2005) reported that each pound of weight lost results in a four-fold reduction in knee joint load per step during daily activities. It has also been suggested that decreases in weight in combination with increased stride lengths result in substantial reductions in knee joint loading (DeVita, Rider, & Hortobagyi, 2016). In contrast, Milner et al. (2018) has suggested that a shorter stride length would reduce the vertical impulse applied to the knee joint, reducing the risk of developing OA. An important difference in these studies pertains to the population of interest. While Milner et al. (2018) focused on obese individuals at a single point in time, DeVita et al. (2016) performed an intervention study and evaluated gait biomechanics across multiple time points in a repeated measures design. The role of step length in knee joint loading has not been well established. There is a need to investigate the role of step length and increasing body mass on knee joint loading rates during gait. Therefore, the purpose of this study is to (a) determine if acutely added mass (weight vest) results in changes in step length during walking, (b) to determine if reduced step length independently (in the absence of added mass) increases knee joint loading, and (c) to determine if added mass results in an increase in knee joint loading. It was hypothesized that: (a) acutely added mass will result in differences in step length (b) reduced step lengths will result in an increase in joint loading, and (c) added mass will alter biomechanical variables and increase joint loading.

Methods

Participants

The location in which this experiment took place was the School of Health Studies Musculoskeletal Analysis Laboratory at the University of Memphis, Tennessee. Participants visited the Musculoskeletal Analysis Laboratory once for examination and testing. The session's duration lasted from 60 to 90 minutes. Prior to any warmup, measurements or testing, individuals were screened for inclusion in this study through the following mechanisms: providing written informed consent, completing a verbal training history to determine study eligibility, and completing a written Physical Activity Readiness Questionnaire (PAR-Q; Appendix A). For each session, testing occurred in the following order: (1) warm-up exercises, (2) placement of measurement sensors, and (3) completion of walking trials including four experimental conditions involving the interaction of two step length conditions and two added mass conditions.

Experimental Equipment

Anthropometric measurements included age, sex, height, and body mass. The following measurements were recorded using a stadiometer and scale. Following anthropometric measurements, retro-reflective markers were placed bilaterally on the participant's lower extremity including the trunk, pelvis, thigh, shank and feet to measure individual segment motion during walking trials (step length x added mass) using a 9-camera motion capture system (240 Hz, Qualisys AB, Goteburg, Sweden). A pair of force platforms were used to record ground reaction forces (GRFs; 1200 Hz, AMTI Inc., Watertown, MA, USA).

Experimental Protocol

All walking trials required the participants to perform eight over-ground walking trials across a 20-meter walkway in each of four experimental conditions. Experimental conditions include the interaction of two step lengths (natural and constrained, 0.68 m) and two weighting conditions (unloaded and loaded) at the participants preferred walking speed. The constrained step length of 0.68 m was selected based on previously published data for obese individuals walking at a self-selected speed (Devita et al., 2016). The self-selected walking velocity was characterized as the pace at which the participant would normally walk during daily activities. The natural step length condition allowed participants to walk with their chosen step lengths while the constrained step length condition required participants to walk with a step length of 0.68 m as outlined on the laboratory floor using masking tape. The unloaded weighted condition was characterized as the participant walking without additional load added onto the participant's body mass. The added mass condition entailed the participants performing the walking trial with an added load of 20% body mass in weighted plates; the plates were placed into a vest worn around the participant's chest. To ensure each participant qualified as "obese" in the added mass conditions, a BMI calculation was performed with the added load to identify if each participant's new BMI exceeded 30 kg/m2 to classify them in the obese category.

A successful walking trial was characterized by the participant walking across the runway at the prescribed velocity and having the foot of interest fully supported by the force platform in the center of the walkway. Participants completed eight successful walking trials per condition totaling 32 walking trials with 60- to 90-second periods of rest between trials to avoid fatigue. Participants wore their active shoe of choice to perform the movements.

Data Analysis

Data captured from the three-dimensional motion capture system were labeled and exported to c3d file. Visual3D (C-Motion, Bethesda, MD, USA) was used to calculate knee joint angle, moment, and power time-series, as well as the knee joint reaction force time-series. Custom software (MatLab, Mathworks, MA, USA) was used to calculate discrete biomechanical variables during the stance phase of gait, including peak knee flexion, knee joint range of motion, peak knee extension moments and powers, and peak positive knee joint reaction force.

Statistics

Five 2 x 2 (load by step length) repeated measures analyses of variance were used to assess the interaction of mass and step length on the following biomechanical variables: peak knee flexion angles, knee joint range of motion, peak knee extension moments, peak knee extension powers and peak knee joint reaction forces. In the presence of a significant interaction or significant main effect, post-hoc paired sample t-tests were used to determine the source of significance. Significance was set at $p < 0.05$.

Results

Table 1 presents the biomechanical variables of interest for each experimental condition including: peak knee flexion angle, knee joint range of motions, peak knee extension moments and powers and peak positive knee joint reaction forces. In Figure 1, no mass by step length interaction was observed for peak knee flexion angles ($p = 0.524$). The constrained step length was associated with greater peak knee flexion angles than the preferred step lengths ($p = 0.043$). Post-hoc t-tests revealed that peak knee flexion angles were greater in the constrained compared to preferred conditions for added mass ($p = 0.03$), but not the unloaded condition ($p = 0.08$). No effect of mass was observed for peak knee flexion angles ($p = 0.578$). In contrast to peak knee flexion angles, no mass-by-step length interaction was observed for knee joint range of motion in Figure 2 ($p = 0.571$). Further, no main effect of step length ($p = 0.299$) or mass ($p = 0.585$) was observed for knee joint range of motion.

Variable	Body Mass			Added Mass		
	Preferred SL	Constrained SL	p-value	Preferred SL	Constrained SL	p-value
Peak Knee Flexion Angle (deg)	-36.0±12.9	-40.5±7.7	0.04	39.0±10.5	-41.4±7.7	0.52
Range of Motion (deg)	40.4±13.2	43.3±6.8	0.30	43.1±10.1	43.9±4.8	0.57
Peak Knee Extension Moment (Nm/kg)	2.9±2.3	2.3±0.8	0.15	2.4±0.7	2.3±0.9	0.31
Peak Knee Extension Power (W/kg)	6.1±4.2	4.6±1.0	0.04	5.7±1.8	4.8±1.0	0.61
Knee Joint Reaction Forces (N/kg)	7.1±2.0	6.1±1.1	0.02	6.9±2.3	5.4±3.1	0.75

Table 1. Biomechanical variables of interest for each experimental condition
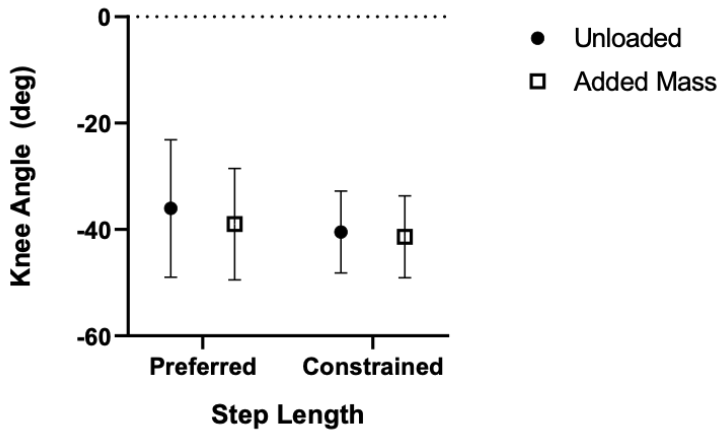
Figure 1. Peak knee flexion (deg) during level walking with increased mass and constrained step lengths. Constrained step length was associated with significant increases in peak knee flexion angles ($p = 0.040$). No changes were observed for added mass ($p = 0.520$).
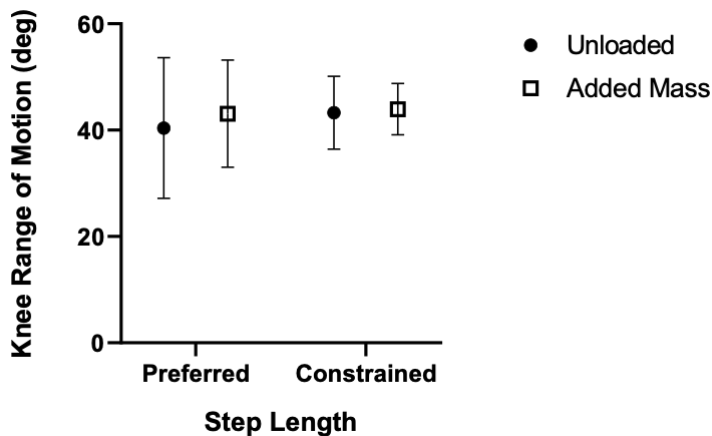
Figure 2. Peak knee range of motion (deg) during level walking with increased mass and constrained step lengths. No changes were observed for added mass (p = 0.57) or constrained step length (p = 0.30).

In Figure 3, no mass by step length interaction was observed for peak knee extension moment (p = 0.306). Further, no main effect of step length (p = 0.153) or mass (p = 0.626) was observed for peak knee extension moment. For peak knee extension power in Figure 4, no mass by step length interaction was observed (p = 0.306). However, a significant main effect of step length was observed (p = 0.037). Post-hoc t-tests revealed that peak knee extension power was greater in the constrained compared to preferred step length conditions for the added mass condition (p = 0.007) but not for the unloaded condition (p = 0.09).
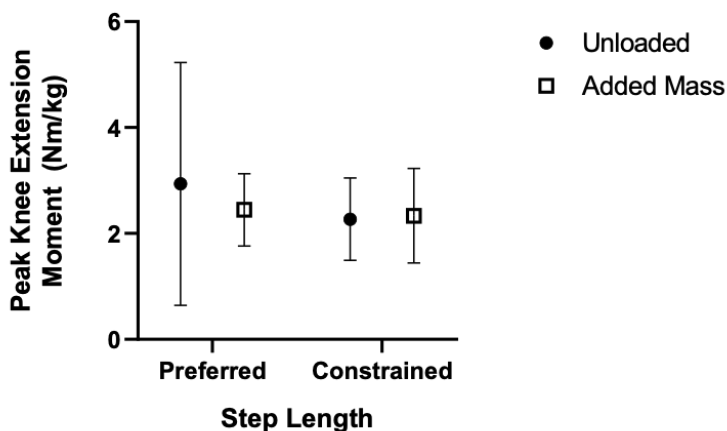
Figure 3. Peak Knee Extension Moment (Nm/kg) during level walking with increased mass and constrained step lengths. No changes were observed for added mass (p = 0.31) or constrained step length (p = 0.15).
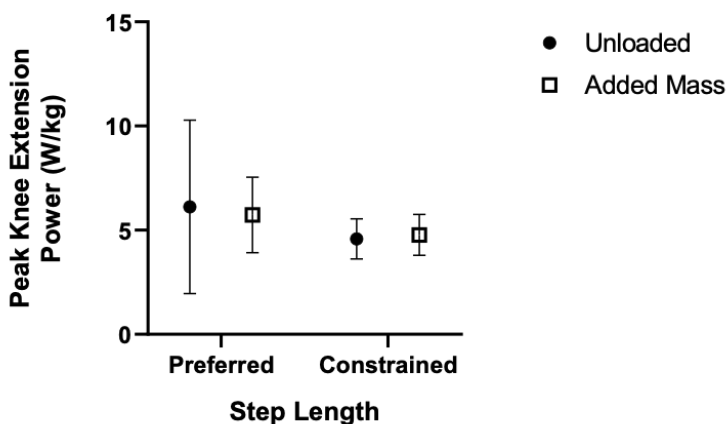

Figure 4. Peak Knee Extension Power (W/kg) during level walking with increased mass and constrained step lengths. Constrained step length was associated with significant increase in peak knee extension power (p = 0.04). No changes were observed for added mass (p = 0.61).

For knee joint reaction forces in Figure 5, no mass by step length interaction was observed (p = 0.753). A main effect of step length was observed (p = 0.019). Post-hoc analyses revealed greater knee joint reaction forces in the preferred compared to constrained step lengths in both unloaded (p = 0.023) and added mass conditions (p = 0.048). No main effect of mass on peak knee joint reaction forces was observed (p = 0.918).
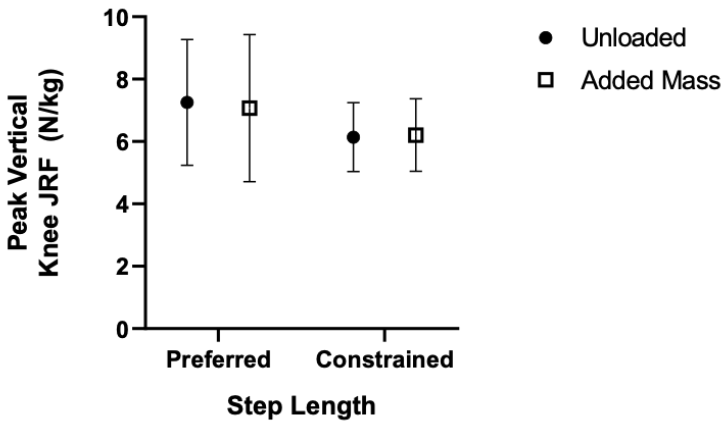

Figure 5. Peak Vertical Joint Reaction Forces (N/kg) during level walking with increased mass and constrained step lengths. Constrained step length was associated with greater knee joint reaction forces (p = 0.02). No changes were observed for added mass (p = 0.75).

Discussion

The purpose of this study was to determine if acutely added mass and/or step length would change knee joint loading during level walking. The major findings of the current study demonstrate that acutely added mass does not alter knee biomechanics; however, constraining step length alters both knee joint kinematics and kinetics. Specifically, constrained step lengths were associated with greater peak knee flexion angles as well as greater joint powers and joint reaction forces.

Current data revealed that acutely added load does not alter knee joint moments and powers during walking. These findings are in contrast with previously published research that demonstrated with added load at the knee during walking, the tasks relative to mass of the individual directly affected joint loads per step and reduced range of motion (Attwells, Birrell, Hooper,

& Mansfield, 2006; Milner et al., 2018). This difference in results can be explained as a chronic versus an acute response, as Messier et al.'s (2005) study was performed in six sessions over an 18-month long weight loss intervention for obese adults. Rather, acute responses to added load have been noted in numerous other studies (Attwells et al., 2006; Knapik, Harman, & Reynolds, 1996). Potential reasons for the differences could be that the added load was not sufficient to create an acute response in recreational athletes. Knapik et al. (1996) started to see significant results at 50% of body weight and up added onto their trained military professionals for kinematic and kinetic differences in walking. This could indicate that a higher stimulus was needed to evoke a difference in our participant population.

However, step length was a strong enough stimulus to evoke a response in knee joint flexion, power, and joint reaction forces. Our findings are supported by Milner et al. (2018), who found that shorter stride lengths reduce knee adduction joint loading. Our results mirror their findings by greater knee joint loads in the preferred step length (i.e., longer step length) compared to the constrained condition. However, our results analyzed different planes of motion compared to Milner et al. (2018) where we analyzed in the sagittal plane (knee flexion) instead of the frontal (knee adduction).

The mechanisms behind the increase in knee joint loading with a longer step length can be defined through kinematic and kinetic variables such as peak knee flexion, extension power, and extension moments. For peak knee flexion, the constrained step length increased under added load compared to the preferred step length condition. Our interpretation is that with an increase in load the subjects adapted to the load by increasing their muscular contribution by flexing the knee, therefore recruiting more muscles to attenuate load. However, this was not represented in the range of motion due to the unaltered state for the constrained added mass condition. This finding is contradicted by Attwells et al. (2006) who found that knee range of motion increases in conjunction to increased load, rather than the knee not changing in range of motion as the load increased. Since range of motion did not change, extension moments at the knee also did not change between conditions, and an increase in flexion was observed. Potentially, our participants walked with their knee more bent, providing a more athletic stance without reaching full extension in between walking phases.

Since there was an increase in peak knee flexion making a more crouched position, an increase of peak knee extension power was potentially due to the increase in force the muscles had to produce while maintaining this flexed position while walking. With the same distance and time the participant had to make a step, the increase in muscle force is a potential source of the increase

in peak knee extension power. While our findings suggest that an increase in muscular contribution to attenuate load helps preserve knee health, past research also states that an increase of load leads to an increase in muscular tension and knee injury (Attwells et al., 2006).

This study has two potential limitations. First, the added mass was applied to the chest region. In obese individuals, accumulative load is seen in alternative areas such as the thigh and lower abdominal regions. This could potentially alter kinematic variables in walking. As shown by Westlake et al. (2013), an increase in thigh circumference alters walking kinematics. If the load was distributed in other regions, such as the thigh, with altered kinematics, we could potentially alter walking kinetics. Another limitation could be that all of our subjects were athletes and not obese individuals. This could affect results since the participants were recreationally active and have an increased ability to adapt to stress unlike the population that this study simulated, obese adults. This was seen by Knapik et al. (1996) who found that foot soldiers did not have altered walking biomechanics until over fifty percent of their body weight was added to their weighted vest. Future studies should look at added load in alternate locations and with different populations to note if a simulated state shows accurate similarity between the two.

The current data demonstrate that increased step length (preferred step length condition) compared to the average preferred obese individuals' step lengthwith or without added mass, decreases the load on the knee. Our findings add to past research that find an increase in stride length could help decrease the risk to skeletal structures by increasing the contributions to muscular components. This information can be applied clinically to individuals with a high risk of OA, such as older and obese populations, to make conscious decisions to increase stride length. However, more studies are needed to investigate simulated obese states to ensure a correlation between 'obese' and 'simulated' investigation data collection structures.

References

Adams, K. F., Schatzkin, A., Harris, T. B., Kipnis, V., Mouw, T., Ballard-Bar-bash, R., . . . Leitzmann, M. F. (2006). Overweight, obesity, and mortality in a large prospective cohort of persons 50 to 71 years old. *N Engl J Med*, *355*(8), 763-778. doi:10.1056/NEJMoa055643

Alley, D. E., & Chang, V. W. (2007). The changing relationship of obesity and disability, 1988-2004. *JAMA*, *298*(17), 2020-2027. doi:10.1001/jama.298.17.2020

Andriacchi, T. P. (1994). Dynamics of knee malalignment. *Orthop Clin North Am*, *25*(3), 395-403. Retrieved from https://www.ncbi.nlm.nih.gov/pubmed/8028883

Attwells, R. L., Birrell, S. A., Hooper, R. H., & Mansfield, N. J. (2006). Influence of carrying heavy loads on soldiers' posture, movements and gait. *Ergonomics*, *49*(14), 1527-1537. doi:10.1080/00140130600757237

Bessesen, D. H. (2008). Update on obesity. *J Clin Endocrinol Metab*, *93*(6), 2027-2034. doi:10.1210/jc.2008-0520

Bliddal, H. (2008). Guidelines for the use of nonsurgical interventions in osteoarthritis management. *Expert Rev Clin Immunol*, *4*(5), 583-590. doi:10.1586/1744666X.4.5.583

Cawley, J., & Meyerhoefer, C. (2012). The medical care costs of obesity: an instrumental variables approach. *J Health Econ*, *31*(1), 219-230. doi:10.1016/j.jhealeco.2011.10.003

DeVita, P., & Hortobagyi, T. (2003). Obesity is not associated with increased knee joint torque and power during level walking. *J Biomech*, *36*(9), 1355-1362. Retrieved from https://www.ncbi.nlm.nih.gov/pubmed/12893044

DeVita, P., Rider, P., & Hortobagyi, T. (2016). Reductions in knee joint forces with weight loss are attenuated by gait adaptations in class III obesity. *Gait Posture*, *45*, 25-30. doi:10.1016/j.gaitpost.2015.12.040

Diseases, N. I. o. D. a. D. a. K. (2017). Overweight & Obesity Statistics. Retrieved from 222.niddk.nih.gov/health-statistics/overweight-obesity

Felson, D. T., Anderson, J. J., Naimark, A., Walker, A. M., & Meenan, R. F. (1988). Obesity and knee osteoarthritis. The Framingham Study. *Ann Intern Med*, *109*(1), 18-24. Retrieved from https://www.ncbi.nlm.nih.gov/pubmed/3377350

Gregg, E. W., Cheng, Y. J., Cadwell, B. L., Imperatore, G., Williams, D. E., Flegal, K. M., . . . Williamson, D. F. (2005). Secular trends in cardiovascular disease risk factors according to body mass index in US adults. *JAMA*, *293*(15), 1868-1874. doi:10.1001/jama.293.15.1868

Haff, G., & Triplett, N. (2016). Nutrition Strategies for Maximizing Performance. In *Essentials of Strength and Conditoning* (4th ed., pp. 218-219). Champaign, IL: Human Kinetics.

Key Health Data About Tennessee. (2018). Trust for America's Health. Retrieved from healthyamericans.org/states/?statid=TN

Knapik, J., Harman, E., & Reynolds, K. (1996). Load carriage using packs: a review of physiological, biomechanical and medical aspects. *Appl Ergon*, *27*(3), 207-216. Retrieved from https://www.ncbi.nlm.nih.gov/pubmed/15677062

Lementowski, P. W., & Zelicof, S. B. (2008). Obesity and osteoarthritis. *Am J Orthop* (Belle Mead NJ), *37*(3), 148-151. Retrieved from https://www.ncbi.nlm.nih.gov/pubmed/18438470

Messier, S. P., Gutekunst, D. J., Davis, C., & DeVita, P. (2005). Weight loss reduces knee-joint loads in overweight and obese older adults with knee osteoarthritis. *Arthritis Rheum*, *52*(7), 2026-2032. doi:10.1002/art.21139

Milner, C. E., Meardon, S. A., Hawkins, J. L., & Willson, J. D. (2018). Walking velocity and step length adjustments affect knee joint contact forces in healthy weight and obese adults. *J Orthop Res*, *36*(10), 2679-2686. doi:10.1002/jor.24031

Mohammed, A., Al-Numair, K. S., & Balakrishnan, A. (2015). Docking studies on the interaction of flavonoids with fat mass and obesity associated protein. *Pak J Pharm Sci*, *28*(5), 1647-1653. Retrieved from https://www.ncbi.nlm.nih.gov/pubmed/26408884

NIH fact Sheets – Osteoarthritis. (2018). Retrieved from report.nih.gov/nihfactsheets/ViewFactSheet.aspx?csid=55

Ruiz, R. (2012). America's Most Obese Cities. Retrieved from www.forbes.com/2007/11/14/health-obesity-cities-forbeslife-cx_rr_1114obese.html.

Sui, X., LaMonte, M. J., Laditka, J. N., Hardin, J. W., Chase, N., Hooker, S. P., & Blair, S. N. (2007). Cardiorespiratory fitness and adiposity as mortality predictors in older adults. *JAMA*, *298*(21), 2507-2516. doi:10.1001/jama.298.21.2507

Tennessee State Obesity Data, Rates and Trends. (2018). Retrieved from stateofobesity.org/states/tn/

Westlake, C. G., Milner, C. E., Zhang, S., & Fitzhugh, E. C. (2013). Do thigh circumference and mass changes alter knee biomechanics during walking? *Gait Posture*, *37*(3), 359-362. doi:10.1016/j.gaitpost.2012.07.031

Yocum, D., Weinhandl, J. T., Fairbrother, J. T., & Zhang, S. (2018). Wide step width reduces knee abduction moment of obese adults during stair negotiation. *J Biomech*, *75*, 138-146. doi:10.1016/j.jbiomech.2018.05.002

Christian Brown is a senior physics and math major from Union University who participated in the Research Experience for Undergraduates at the University of Memphis in the summer of 2019. He worked under Dr. Francisco Muller Sanchez over a 10-week period. In the future, Christian plans to pursue a graduate degree in physics after completing his undergraduate degree.

Christian Brown

Physical Characteristics of the Nuclear Region of NGC 4388

Faculty Sponsor

Dr. Francisco Muller Sanchez

Abstract

Several observed relationships between black holes and galaxies show that growth of supermassive black holes relates to galaxy evolution. These relations can be addressed by studying feeding and feedback. The KONA survey observed the core region of the Seyfert 2 galaxy NGC 4388 in the near-IR spectrum (1.963-2.379 μm). The OSIRIS IFS produced a datacube of a 3.3" x 4.7" region containing the AGN. Gaussian curves were fitted to the peaks of Si VI, H_2 1-0 S(1), and Brγ with QFitsView. QFitsView and Astropy were then used to produce, mask, and smooth the flux, velocity, and dispersion maps for the peaks. The Si VI and Brγ maps showed evidence of an outflow in the south, while H_2 1-0 S(1) showed evidence of a warped disk, rotation, and behavior linked to the torus. Behavior of Si VI and Brγ in the north is likely linked to a ram pressure stripping event.

Introduction

The most powerful and luminous objects in the known universe, supermassive black holes (SMBH) reside at the center of galaxies and can measure up to billions of solar masses. Many observed relationships between black holes and their host galaxies indicate a close connection between the formation of the two (Heckman & Best 2014). Understanding the behavior and structure of the material in the central regions of Seyfert galaxies is undoubtedly critical to the understanding of the nature of these objects due to their incredible influence on the material. Certain phenomena such as inflows and outflows are especially important to discerning an accurate description of galactic nuclei and how the material in them interacts with the SMBH. This, in turn, would also shed light on the nature of the coevolution of galaxies and SMBHs.

The Keck OSIRIS Nearby AGN (KONA) survey (Müller-Sánchez et al.), which sought to study the nuclear kinematic structure of 40 nearby active galaxies through the Keck Telescope and OSIRIS near-infrared integral field spectrograph, was conducted with the goal of researching several of these Seyfert galaxies. NGC 4388 is one galaxy observed in this survey. It is a barred spiral galaxy that is almost edge on in its inclination ($i \approx 78°$) (Veilleux et al.). It is a Seyfert 2 galaxy located in the Virgo Cluster (Phillips et al.) with a redshift z = 0.00842 (Lu et al.). It is near the center of the cluster and one of the brightest in the cluster with a magnitude of M_r = -20.1.

The galaxy has an active galactic nuclei (AGN) and shows evidence of a very extended emission line region (VEELR) that reaches to roughly 35 kpc to the northeast of the galactic plane (Yoshida et al.). This is possibly due to past interactions with other galaxies. Evidence of a ram pressure stripping event around 200 Myr ago that pulled material off of the galaxy adds credibility to this scenario (Vollmer et al.).

There is kinematic evidence for a misaligned nuclear disk near the core of the galaxy (Greene et al.). This disk in the central 1° is misaligned by 15° from the main disk of the galaxy. Additionally, there is a maser disk, or source of a high level of stimulated spectral line emission, on the sub-pc scale (Braatz et al.). The galaxy shows uniform rotation in the H_2 spectrum in the plane of the galaxy, but Brγ and Si VI do not show this behavior (Greene et al.).

Observations and Methods

The KONA survey utilized the Keck observatory in Hawaii with the OSIRIS integrated field spectrometer (IFS) to observe NGC 4388 in the near-IR spectrum (1.963-2.379 μm). The observation was done on December 15,

2016, with a scale of 0.05 arcsec/pixel. A region of 66 x 94 pixels was observed. The observation was done under good atmospheric conditions with an airmass of 1.15. The collected data was stored in a .fits file datacube.

QFitsView was utilized to analyze the datacube. The emission peaks for Si VI, H_2 1-0 S(1), and Brγ were identified for spectra at several different locations. Gaussian peaks were then fitted to these peaks. QFitsView was then used to automatically produce flux, velocity, and dispersion maps for these emissions centered on the wavelengths of these peaks at the central location. QFitsView produced flux maps based on the intensity of the peak at each pixel, velocity maps based the shift in wavelength of the center of the peak from the wavelength at the central position, and dispersion maps measured the full width at half maximum (FWHM) of the peak at each location. The starting parameters for Si VI were a center of 1.978187 μm and FWHM of 130 km/s for Si VI, 2.137739 μm and 230 km/s for H_2 1-0 S(1), and 2.182589 μm and 190 km/s for Brγ.

The Astropy package in Python (Robitaille et al.) was then used to analyze the maps produced by QFitsView. Noise was filtered out by first removing pixels with unusually high or low values that did not fit into any physical structure. This was done by masking the maps with themselves in certain regions and choosing minimum and maximum values that were automatically replaced with a low value, 1 for velocity and dispersion maps and 0.01 for flux maps. A Gaussian smoothing function was applied to the maps and then another mask was applied using a smoothed continuum image to remove further noise in the extremes of the image. Flux maps were then normalized to the brightest pixel in each map. A rotational model was then produced for velocity maps with rotational motion. The model is in the form

$$V_{los} = \sqrt{\frac{R^2 GM}{(R^2 + A^2)^{\frac{3}{2}}}} \frac{sin(i)\ cos(\psi - \psi_0)}{\left(cos^2(\psi - \psi_0) + \frac{sin^2\ (\psi - \psi_0)}{cos^2(i)}\right)^{\frac{3}{4}}}$$

where R is the radial coordinate, ψ is the angular coordinate, V_{los} is the velocity in the line of sight of the observer, G is the gravitational constant, i is the inclination, M is mass, A is the correspondent scale length to R, and ψ is the angular tilt of the plane. The velocity maps were then subtracted from this model to create residuals.

Results

Location peak (x, y)	Flux	Height	Center	FWHM
(12, 60)				
Si VI	118.509	0.839419	1.448645	132.629
H$_2$ 1-0 S(1)	399.924	1.70203	58.68266	220.738
Brγ	120.078	1.02774	23.37855	109.761
(21, 60)				
Si VI	186.494	1.11297	-21.46072	157.417
H$_2$ 1-0 S(1)	334.757	1.35027	71.83225	232.903
Brγ	115.336	0.583478	4.66206	185.747
(28, 71)				
Si VI	172.653	1.11093	-13.7718	146
H$_2$ 1-0 S(1)	142.555	0.473062	3.049578	283.094
Brγ	158.197	0.481341	-11.88695	308.755
(33, 60)				
Si VI	2556.6	18.3413	0.00070061	130.948
H$_2$ 1-0 S(1)	1089.83	4.34282	-5.151806	235.752
Brγ	942.452	4.7224	0.07014403	187.484

Location peak (x, y)	Flux	Height	Center	FWHM
(36, 49)				
Si VI	527.624	1.98357	40.91657	249.888
H$_2$ 1-0 S(1)	99.2693	0.419417	-8.000039	222.349
Brγ	124.587	0.538189	48.8313	217.473
(41, 37)				
Si VI	260.25	0.799837	-63.60072	305.673
H$_2$ 1-0 S(1)	68.0861	0.226325	-73.91846	282.614
Brγ	164.192	0.315791	-74.13898	488.448
(45, 60)				
Si VI	1184.33	2.59361	-18.04886	428.98
H$_2$ 1-0 S(1)	159.004	0.683473	-46.06937	218.552
Brγ	120.058	0.431776	-13.00337	261.217
(54, 60)				
Si VI	1399.58	2.78901	-101.4793	471.429
H$_2$ 1-0 S(1)	513.729	1.84718	-58.95029	261.273
Brγ	90.5817	0.267641	-50.87357	3917.947

Table 1. Results from Gaussian fits of Si VI, H$_2$ 1-0 S(1), and Brγ peaks at the given locations in velocity space. Each velocity space is centered on the wavelength of the peak at the central region.

Utilizing QFitsView, spectra were extracted from several regions of the galaxy. A diagram of this is shown in Figure 1. The following peaks were visible in the spectra: H_2 1-0 S(3), Si VI, He I, H_2 1-0 S(2), H_2 1-0 S(1), Brγ, Ca VIII, H_2 1-0 S(0). The central spectra shows a slope near 0 with very prominent, narrow emission lines. Moving away from the center, the spectrum shows a more negative slope. The individual peaks of Si VI, H_2 1-0 S(1), and Brγ, were analyzed at these locations as well, with Gaussian curves being fitted to these peaks. The results are shown in Figures 2, 3, and 4, with the results of the Gaussian fits being shown in Table 1.

The Si VI peak broadens to the east and south sections of the map. It shows a tail of blueshift north of the AGN and slightly to the west. Slightly south of the core shows a redshifted behavior while further south shows blueshift.

H_2 1-0 S(1) shows redshift to west and blueshift to the east. There is some visible broadening to the north and east portions of the map. The V/σ map has very low values, with a maximum of around 0.4, but does grow in magnitude towards the eastern and western extremes.

Brγ shows strong broadening to the south and east as well as some redshift slightly south of the nucleus. Much of the behavior far from the core may be due to atmospheric noise.

Finally, QFitsView was used to produce flux, velocity, and dispersion maps by automatically analyzing the intensity, redshift, and full width at half maximum (FWHM) of the peak at each pixel in the observed region.

Once Astropy was utilized to mask and smooth the maps, and normalize the flux maps, they were plotted as images.

The Si VI flux map shows an extremely bright center with some spots of high intensity throughout the disk, but none of these show a flux higher than 0.16. The velocity map shows very little motion in the disk, but some slight blueshift north of the disk, and an area of noticeably high redshift to the south and very high blueshift further south and slightly east. The dispersion map shows an area of dispersion over 400 km/s south of the AGN as well as areas of lower dispersion to the northwest.
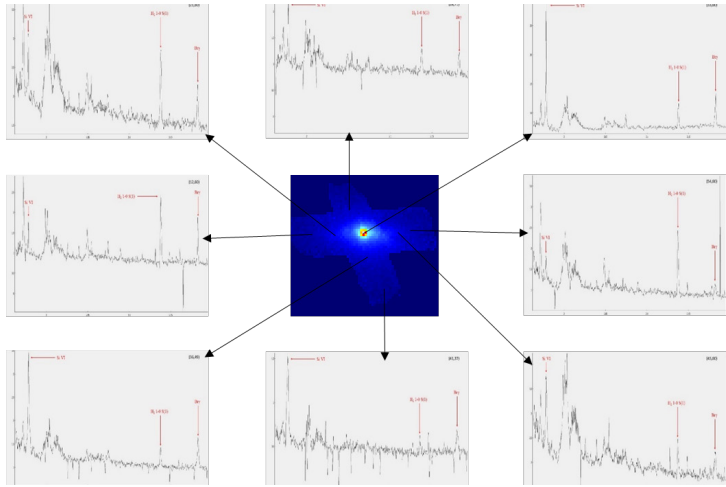
Figure 1. A continuum image of the galaxy (center), with spectra from the following postions (starting top right and going clockwise. Coordinates relative to center in form of (R.A., Dec.)): (0", 0"), (1.05", 0), (0.6", 1.05"), (-0.4, -1.15), (-0.15", -0.55"), (-0.6", 0"), (-1.05", 0"), (0.25", 0.55"). Each spectrum shows the region (1.963-2.195 μm) and was extracted from a region with a pixel radius of 3. The peaks for Si VI, H_2 1-0 S(1), and Brγ are labeled on each spectrum.
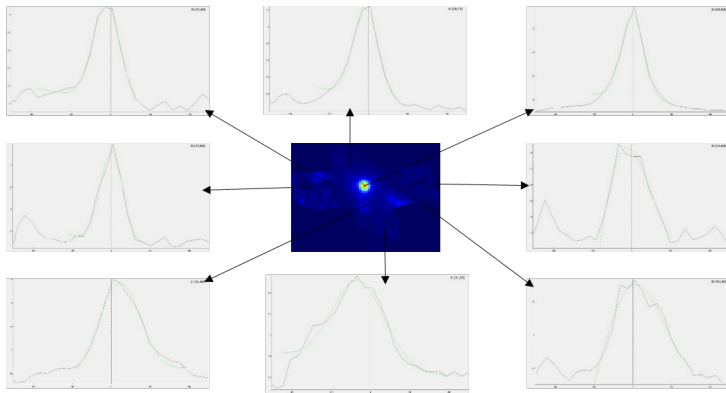

Figure 2. Same alignment as Figure 1 but showing the flux map for Si VI in the center and the spectrum peak for Si VI at each location. The spectra are in velocity space from -500 to 500 km/s, centered at 1.978187 μm. A dotted line is shown on each spectrum to indicate this central position. Each peak is also shown with an approximate Gaussian fit.
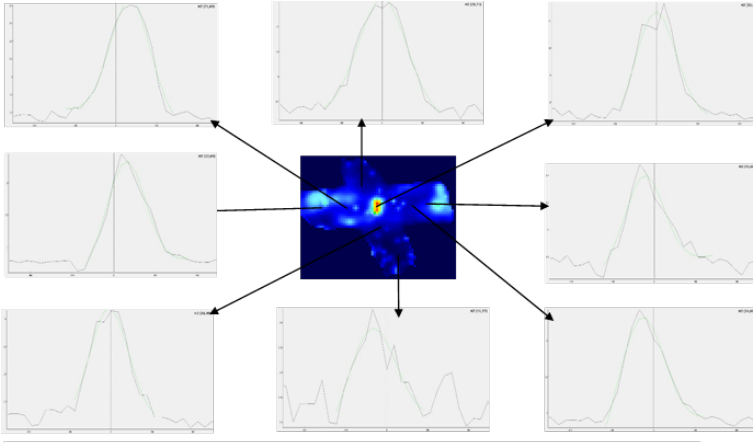
Figure 3. Same as Figure 2 but showing H$_2$ 1-0 S(1) flux map and spectra peaks, centered at 2.137739 μm.
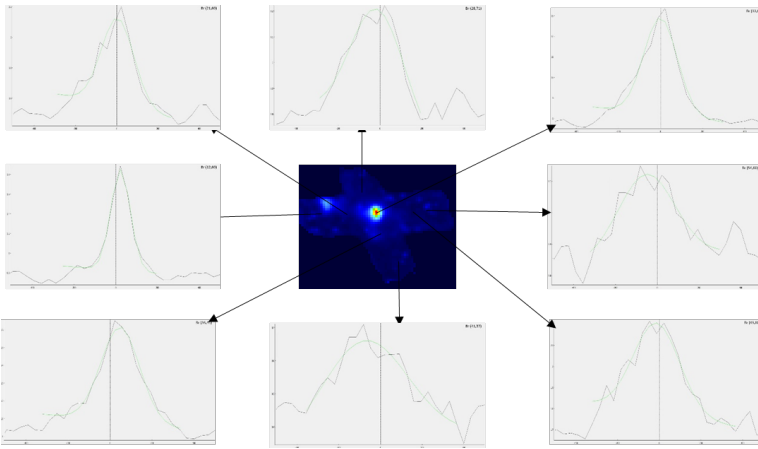
Figure 4. Same as Figure 2 but showing Brγ flux map and spectra peaks, centered at 2.182589 μm.

The H$_2$ 1-0 S(1) flux map has a bright center, and areas of high flux within the disk both to the west and far east. The velocity map reveals a clear gradient in the disk from redshift in the west to blueshift in the east, along with some areas of slight blueshift to the far south. The dispersion map reveals spots of high dispersion scattered throughout the disk that seem to be spatially coincident with areas of low flux.
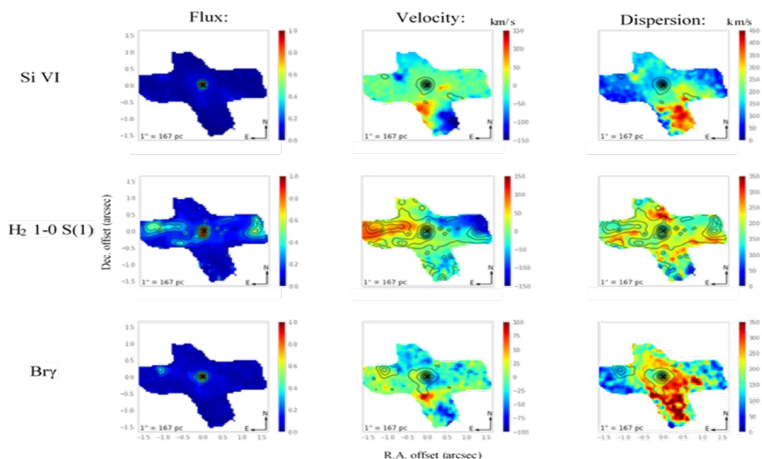
Figure 5. Flux, velocity, and FWHM dispersion maps for Si VI, H$_2$ 1-0 S(1), and Brγ. All maps are plotted with the contours from that peak's flux map, with contours ranging from 0 to 1 on intervals of 0.1. A black *x* marks the estimated location of the AGN.
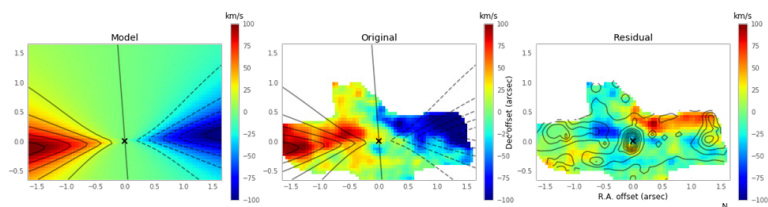
Figure 6. Shown are the model (left), H$_2$ 1-0 S(1) velocity map with contours of the model overlaid (center), and the residual with contours of H$_2$ 1-0 S(1) flux overlaid. The bottom section of the maps was cut to remove data that was not part of the rotational structure.

The velocity map shows similar structure to Si VI with relatively little activity in the disk, but a slight blueshift in the north, with an area of higher redshift to the south and high blueshift further southeast. The dispersion map has a ring-shaped structure of high dispersion surrounding the nucleus with extremely high dispersion in the south.

The Brγ flux map has a bright center with another small area of high intensity to the west. The velocity and dispersion maps are very similar to those of Si VI but with a lower magnitude. There is also slightly more evidence of motion and dispersion within the galaxy plane.

67
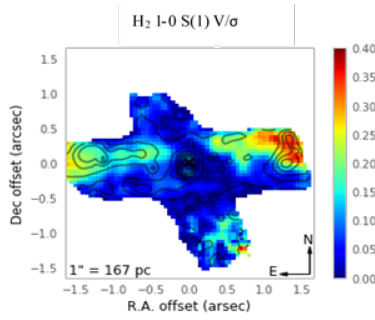
Figure 7. A map of the ratio of velocity and sigma for H$_2$ 1-0 S(1) over-laid with the same H$_2$ 1-0 S(1) flux contours as figure 5.
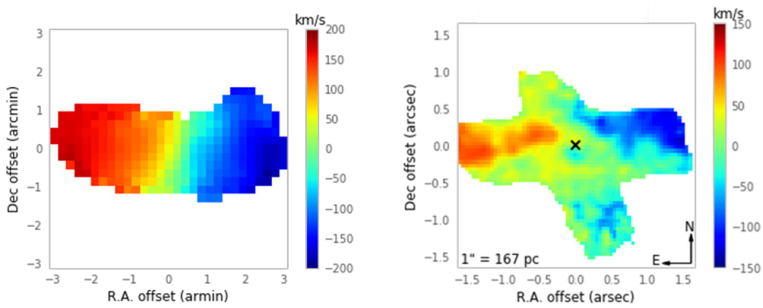

Figure 8. On the left is a velocity map from VIVA on the kiloparsec scale of NGC 4388. On the right is the KONA H$_2$ 1-0 S(1) velocity map on scale of 10's of parsecs. The angle of rotation for the inner area is measured to be around 82 degrees from south for the VIVA image and approximately 96 degrees from south on the KONA map. A black line has been added tracing the angle of rotation for each.
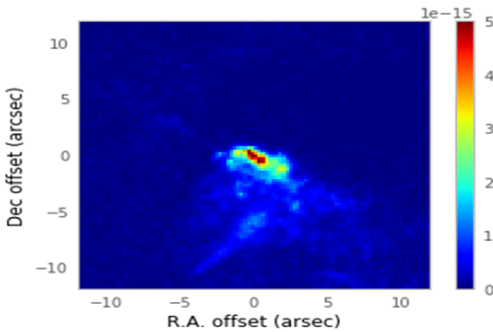
Figure 9. A Hubble Space Telescope image showing the OIII flux of NGC 4388. The ionization cone south of the nucleus is clearly visible.

A kinematic model in the form of

$$V_{los} = \sqrt{\frac{R^2 GM}{(R^2 + A^2)^{\frac{3}{2}}}} \quad \frac{\sin(i)\cos(\psi - \psi_0)}{\left(\cos^2(\psi - \psi_0) + \frac{\sin^2(\psi - \psi_0)}{\cos^2(i)}\right)^{\frac{3}{4}}}$$

was created with values of A = 300 pc, M = 2.5* 109 M, and 0 = 0.075 radians. These values were estimated using a X2 minimization. The center of rotation is placed on the location of the AGN, and the maximum velocity within our domain is 107.5 km/s. The H_2 1-0 S(1) velocity map was then subtracted from this model to produce a residue. These results are shown in Figure 7.

Discussion

The position of the AGN was determined via level of intensity. Each continuum and flux map consistently showed the most luminous pixel in the center to be located at pixel (33, 60).

The H_2 1-0 S(1) velocity map shows strong evidence of rotation in the plane of the galaxy. This is consistent with observations done on larger scales, as well as stellar rotation (Greene et al.). However, this rotation is at a different angle from rotation at larger scales. Figure 8 shows an image from VIVA (Chung et al.) on the kiloparsec scale compared to one of our images and clearly shows an offset of around 14 degrees between the two images. This offset disk has been suggested by past observations (Greene et al.).

The V/σ map for H_2 1-0 S(1) shows relatively low values, indicating a thick disk. This combined with the aforementioned misaligned disk of rotation suggest it is aligned with the maser disk. Thus, the behavior of H_2 is associated with the torus.

The maps of Si VI and Brγ show evidence for strong behavior south of the galactic plane. The dispersion for both is extremely high in this region, with Si VI having dispersion above 400 km/s at some spots. The velocities of both also show strong behavior in this region, with both having an area of high redshifted velocity and blueshifted in similar regions. Brγ does show high areas of dispersion around the nucleus that Si VI does not, showing it may be more prevalent in the disk of the galaxy. These observations are consistent with results from observations on slightly larger scales (Greene et al.). The motion of Si VI and Brγ indicate the ionized gas in the south of NGC 4388 is likely due to an outflow. Paired with the observations of a radio jet and ionized gas south of the galaxy (Falcke et al.), this indicates the presence of an outflow from the AGN. The ionization cone can be seen in Figure 9.

The H_2 1-0 S(1) velocity and dispersion maps, while weaker, also show some activity in the south with the velocity being blueshifted and dispersion showing spots of high activity. This could be evidence that some molecular gas is also involved in the outflow.

The northern section of the maps do not show as much activity as the southern part. This is due in part to some of the region being removed during the masking process due to noisy data. However, it still does show a slight blueshift in the Si VI and Brγ velocity map. The dispersion maps for these two peaks also show some mild activity, while the H_2 1-0 S(1) dispersion map shows a spot of high activity in this region. Such behavior does not seem to be consistent with what is occurring in the south of the galaxy. A likely explanation for this is a ram pressure stripping event. It has already been shown that NGC 4388 likely went through such an event around 200 Myr

ago (Vollmer et al.). The effects of this event are likely tied to the behavior seen in the north of NGC 4388.

Conclusions

Data analysis of NGC 4388 revealed several things. The previously observed ionization cone and radio jet at the south of the galaxy is likely the result of an outflow from the AGN. This is most clearly seen in the dispersion and velocity maps of Si VI and Brγ, with some possible molecular gas also present as seen in the velocity and dispersion maps of H_2 1-0 S(1). The H_2 1-0 S(1) velocity map shows clear evidence of rotation within the disk of NGC 4388. However, this does not appear to be pure rotation. The angle of rotation does not line up with the angle seen from observations of the galaxy on larger scales. This is strong evidence for a warped disk in the inner region. The small values of H_2 1-0 S(1) V/σ near the center suggest H_2 behavior is associated with the torus. Small blueshifted motion and low-level dispersion in the north of the galaxy are likely the result of NGC 4388 undergoing a ram pressure stripping event at some point in the past.

References

Braatz, J. A. et al. "A Green Bank Telescope Search for Water Masers in Nearby Active Galactic Nuclei." The Astrophysical Journal 617.1 (2004): L29–L32. Crossref. Web.

Chung, Aeree et al. "Erratum: 'VLA Imaging of Virgo Spirals in Atomic Gas (Viva). I. The Atlas and the H I Properties." The Astronomical Journal 139.6 (2010): 2716–2718. Crossref. Web.

Greene, Jenny E. et al. "Circumnuclear Molecular Gas in Megamaser Disk Galaxies NGC 4388 and NGC 1194." The Astrophysical Journal 788.2 (2014): 145. Crossref. Web.

Heckman, Timothy M. and Best, Philip N. " The Coevolution of Galaxies and Supermassive Black Holes: Insights from Surveys of the Contemporary Universe." Annual Review of Astronomy and Astrophysics 52.1 (2014): 589-660. Crossref. Web

Falcke, Heino, Andrew S. Wilson, and Chris Simpson. "Hubble Space Telescope and VLA Observations of Seyfert 2 Galaxies: The Relationship Between Radio Ejecta and the Narrow-Line Region." The Astrophysical Journal 502.1 (1998): 199–217. Crossref. Web.

Lu, N. Y., Hoffman, G. L., Groff, T., Roos, T., Lamphier, C. "H i 21 Centimeter Observations and I-Band CCD Surface Photometry of Spiral Galaxies behind the Virgo Cluster and toward Its Antipode." Astrophysical Journal Supplement v.88 (1993): 383-413. Crossref. Web.

Müller-Sánchez, F. et al. "The Keck/OSIRIS Nearby AGN Survey (KONA). I. The Nuclear K-Band Properties of Nearby AGN." The Astrophysical Journal 858.1 (2018): 48. Crossref. Web.

Phillips, M.M. and Malin, D.F. "NGC 4388: a Seyfert 2 galaxy in the Virgo cluster." Mon. Not. R. Astr. Soc. 199.4 (1982) 199, 905-913. Crossref. Web.

Robitaille, T. P. et al. "Astropy: A community Python package for astronomy." A&A 558, A33 (2013): 1432-0746. Crossref. Web.

Veilleux, S., J. Bland-Hawthorn, and G. Cecil. "A Kinematic Link Between Boxy Bulges, Stellar Bars, and Nuclear Activity in NGC 3079 and NGC 4388." The Astronomical Journal 118.5 (1999): 2108–2122. Crossref. Web.

Vollmer, B. et al. "Two Uneven Sisters." Astronomy & Astrophysics 620 (2018): A108. Crossref. Web.

Yoshida, Michitoshi et al. "Discovery of a Very Extended Emission-Line Region Around the Seyfert 2 Galaxy NGC 4388." The Astrophysical Journal 567.1 (2002): 118–129. Crossref. Web.

Daniel Duong completed his B.S. in physics from the University of West Florida in August 2019. He was a member of the Society of Physics Students as well as the head of media for the Baptist Collegiate Ministries. Daniel was also involved in computation physics research under Dr. Christopher Varney. Over the summer of 2018, Daniel received an opportunity to conduct research under Dr. Firouzeh Sabri at the University of Memphis through the Research Experience for Undergraduates program funded by the National Science Foundation.

Daniel Duong
The Synthesis and Preparation of Upconverting and Downconverting Phosphors for Sensing Applications

Faculty Sponsor
Dr. Firouzeh Sabri

Introduction

Thermometry has always been important for scientific and industrial applications. Its usage ranges from environment sensing and climate control to medical uses. Thermometry plays an important role in determining if a region of space is suitable to the application at hand, from habitable conditions and possible hazards to the usage of electronics. It helps determine how certain materials will behave, thus informing the best way to prepare accordingly.

Just as the applications of thermometry have a wide array, so are the types of thermometry, each with their respective strengths and weaknesses. One type of thermometry uses thermal expansion. A classic example of this would be the mercury thermometer. The mercury expands as it is heated, and the volume is then used to determine the temperature. While useful for a broad range of applications, a downside is that it must be in contact with the material itself. Other types of thermometry require a medium to travel through, are not highly accurate, or cannot detect a wide range of temperatures (Aryal, 2018). For the purposes of space exploration and settlement, these factors play a significant role in determining the type of thermometry used. As a result, phosphor thermometry is a strong contender to be the best way to deal with these issues.

Phosphor thermometry operates by using photoluminescence, thus avoiding all of the issues above. This occurs by shooting a short pulse laser at the phosphor, enabling the electrons to reach an excited state, and measuring the emissions from the electrons as they fall back to ground level (Aryal, 2018). This is why the phosphors are described as upconverting and downconverting. For the purposes of this experiment, the decay rate will be used to determine the temperature, as it is the most widely-used method, and a method which is compatible with a configuration which will be stated later (Allison et al, 2017). Phosphor thermometry does have one weakness, however. The phosphors are in powder form, which makes them difficult to handle.

Due to their small particle size, a variety of issues arise. They will easily cross contaminate with other materials, messing up measurements. In addition, their high surface charge causes them to adhere to most materials as well as cluster together, creating a non-uniform amount of the powder for sensing. Outside forces will cause the powder to disperse. In this form, the phosphor powders are hazardous, not only to people, but also to the environment, therefore necessitating Environmental Protection Agency regulations. Lastly, the phosphors are reusable, but not recoverable in this state, and can only be utilized on a limited number of surfaces (Rietema, 1991). Thus, the proposed

solution is to encapsulate the powders in Sylgard 184.

Sylgard 184 is classified under the family of polydimethylsiloxane (PDMS). PDMS is a common elastomer used for space exploration due to its insulating abilities, flexibility, non-flammability, and easy synthesis. Especially critical in this experiment is PDMS's characteristic of being inert (Fontenot et al, 2016). This allows it to be doped with different materials, enabling the creation of composites. By forming a composite with the phosphor powders, the phosphor itself becomes easier to handle and thus, more applicable. PDMS is also transparent in the visible spectrum, thereby not distorting the photoluminescence of the phosphor powders (Allison et al, 2017).

The purpose of this experiment is to create a method in which the phosphor powders can be reliably encapsulated without the loss of the powder. In addition, the identification of the best suited temperature dependent bandwidths will be identified. Finally, an investigation was made to see if the encapsulation process had any effect on the excitation or emission behavior of each compound.

Materials

Thirteen different phosphor powders were acquired for this research. Eight of the powders were acquired from Intelligent Materials, and the other five were acquired from the University of Louisiana, Lafayette. The powders acquired from Intelligent Materials were Yttrium, Lanthanum, Lanthanum/Gadolinium, 620 Nitrate, 630 Nitrate, Zinc Sulfide UV (Green), Bismuth, and Zinc Sulfide UV (Blue). From the University of Louisiana, Lafayette, three Europium Tetrakis powders and two Magnesium Tetrakis powders were acquired (Fontenot et al, 2012; 2015). Sylgard 184 was used as the encapsulation elastomer.

Procedures

The same general procedure was followed for the majority of the composites. First, Sylgard 184 and the curing agent were mixed at a ratio of ten to one to form PDMS. This ratio was predetermined by previous experiments. Following this, the sample was outgassed for four to five minutes. The PDMS was mixed with the phosphor powder at a ratio of twenty-two to one and mixed by hand thoroughly for three to four minutes. The sample was outgassed a second time for four to five minutes. Within the next three to four minutes, the mixture was poured into the dog bone mold and outgassed completely. Lastly, it was cured in an oven at 100 °C for an hour, cooled, and removed from the mold. Aside from this synthesis method, the Europium Tetrakis was

ground from crystals into a powder. As for Bismuth, an eighty-micrometer sieve was utilized to acquire a more homogeneous powder size.

To measure the photoluminescence of the powders, a 405-nanometer laser was first used to excite the electrons. A PDMS layer of 6.26-millimeter thickness was placed on top of the powders. The function generator was set with a square wave at a 1.5 millisecond pulse. A photomultiplier was placed to detect the luminescence of the powders. A variety of lenses were used in order to determine the temperature dependent bandwidths. The stage was connected to the temperature controller in order to vary the temperature of the powders. The powders were given five minutes to rise to the desired temperature if the temperature increment was five degrees Celsius, and eight minutes if the increment was ten degrees Celsius. The photomultiplier was then output into an oscilloscope in order to see the decay of the photoluminescence. From there, the decay rate of each of the powders at elevated temperatures were determined.

The exact same procedures were utilized to determine the decay rates of the composites. One exception is for the Zinc Sulfide UV (Green) for both the powder and composite form: a pulse length of 2.0 millisecond pulse length was utilized since it took the powders longer to reach a steady excited state. For the phosphors with the decay rates that were analyzable at room temperature, they were tested from room temperature to 200 degrees Celsius in five- or ten-degree increments.

Results

For the majority of the phosphor powders, they were successfully encapsulated into PDMS. Table 1 displays which materials were cured successfully and which were not. Other methods of curing were also tested on the Lanthanum/Gadolinium samples such as curing at 200 degrees Celsius and using UV curing. Unfortunately, neither of these methods worked. The composites remained liquid, indicating the powders were interfering with the curing chemical reaction. For the successfully cured samples, the physical characteristics of each composite varied and should be investigated at a later date.

Phosphor Powder	Successful Curing?
1: Yttrium	Yes
2: Lanthanum	Yes
3: Lanthanum/Gadolinium	No
4: 620 Nitrate	Yes
5: 630 Nitrate	Yes
6: Zinc Sulfide UV (Green)	Yes
7: Bismuth	No
8: Zinc Sulfide UV (Blue)	Yes
B: Europium Tetrakis #1	Yes
C: Europium Tetrakis #2	Yes
D: Europium Tetrakis #3	Yes
F: Magnesium Tetrakis #1	Yes
G: Magnesium Tetrakis #2	Yes

Table 1. Curing Composites

Next, the optimal wavelengths for each phosphor were observed and recorded. Table 2 shows which wavelength lens should be used for each phosphor.

Phosphor Powder	Optimal Wavelength
1: Yttrium	460 nm
2: Lanthanum	460 nm
3: Lanthanum/Gadolinium	460 nm
4: 620 Nitrate	650 nm
5: 630 Nitrate	650 nm
6: Zinc Sulfide UV (Green)	540 nm
7: Bismuth	540 nm
8: Zinc Sulfide UV (Blue)	460 nm
B: Europium Tetrakis #1	650 nm
C: Europium Tetrakis #2	650 nm
D: Europium Tetrakis #3	650 nm
F: Magnesium Tetrakis #1	460 nm
G: Magnesium Tetrakis #2	460 nm

Table 2. Powders and Composites Optimal Wavelength

The optimal wavelength was determined by selecting the most prevalent and analyzable decay rates. An example can be seen in Figure 1.
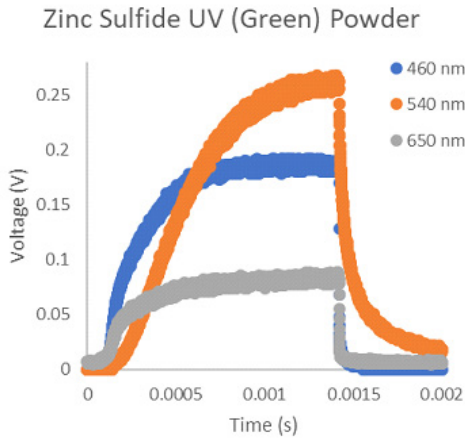
Figure 1. The decay rate for Zinc Sulfide UV (Green) Powder is shown above. It displays the amount of voltage against time.

From the figure above, it can be determined that the optimal wavelength for Zinc Sulfide UV (Green) is 540 nm due to the longer decay time. In addition, both the powders and the phosphors had the same optimal wavelengths. This is evident in Figure 2.
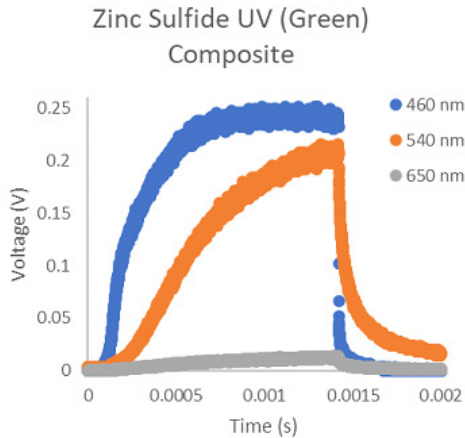

Figure 2. The decay rate for Zinc Sulfide UV (Green) Composite. It displays the amount of voltage against time.

Lastly, when setting up the decay behavior of the photo luminescence against the natural logarithm of the temperature, the same linear lines were evident between the powders and their respective composites. The standard data is seen in Figure 3.
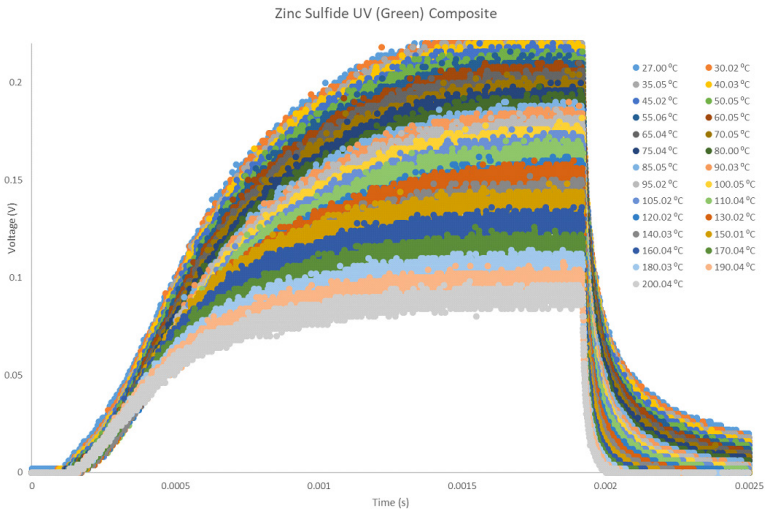
Figure 3. The decay rates for various elevated temperatures for Zinc Sulfide UV (Green) Composite using a 540-nanometer wavelength lens. A look at the data shows that higher temperatures are correlated with shorted decay rates.

When plotted in a log plot, the linearity of the correlation can be seen.
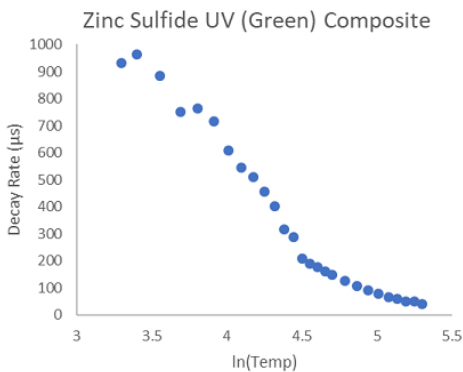
Figure 4. The decay rates plotted against the natural logarithm of the temperature. This is for the Zinc Sulfide UV (Green) Composite.

There also appears to be two separate linear sections in the correlation, which should be investigated at a further date. The Zinc powder and the Europium Tetrakis samples were also measured and a linear correlation is also seen. All of the other composites' decay rates were too short to measure at elevated temperatures.

Conclusion

The majority of the powders were successfully encapsulated by PDMS into composite form. In addition, the encapsulation process does not affect the readings on the decay rates. As a result, the benefits of the phosphor powders are retained while the weaknesses are eliminated. With the optimal wavelengths analyzed, the correct lens can be chosen to observe each phosphor powder.

As the composites have been analyzed, the phosphor samples can be used as a temperature sensing apparatus. The composites can be utilized where traditional methods of thermometry are lacking. Since taking readings is non-contact, accurate, and quick, this form of thermometry has many advantages, and one of the best utilizations is in space applications where conditions make temperature readings difficult.

In the future, it would be desirable to see lower temperatures explored. In addition, other characteristic tests of the composites would be useful, as while the effects of PDMS on the powders have been observed to an extent, the effects on the characteristics of PDMS has not. The potential of temperature flux has not been analyzed. It can be achieved by layering the different composites on top of each other and reading the different decay rates. Finally, encapsulation of the powders in other materials such as aerogels would be useful for future study.

References

Allison, S. W., Baker, E. S., Lynch, K. J., & Sabri, F. (2017). In vivo X-Ray excited optical luminescence from phosphor-doped aerogel and Sylgard 184 composites. *Radiation Physics and Chemistry*, *135*, 88–93. doi: 10.1016/j.radphyschem.2017.01.045

Fontenot, R. S., Bhat, K. N., Hollerman, W. A., Aggarwal, M. D., & Nguyen, K. M. (2012). Comparison of the triboluminescent yield and decay time for europium dibenzoylmethide triethylammonium synthesized using different solvents. *CrystEngComm*, *14*(4), 1382–1386. doi: 10.1039/c2ce06277a

Fontenot, R. S., Owens, C. A., Bhat, K. N., Hollerman, W. A., & Aggarwal, M. D. (2015). Magnesium tetrakis dibenzoylmethide triethylammonium: A novel blue emitting phosphor. *Materials Letters*, *146*, 9–11. doi: 10.1016/j.matlet.2015.01.141

Fontenot, R. S., Allison, S. W., Lynch, K. J., Hollerman, W. A., & Sabri, F. (2016). Mechanical, spectral, and luminescence properties of ZnS:Mn doped PDMS. *Journal of Luminescence*, *170*, 194–199. doi: 10.1016/j.jlumin.2015.10.047

Rietema, K. (1991). *The Dynamics of Fine Powders*. Elsevier Applied Science.

Aryal, M. (2018). Heat flux calculations of PDMS and silica aerogel through phosphor thermometry. [Master thesis, University of Memphis]

Jacob Parks is currently an undergraduate student double majoring in physics and mathematical sciences at the University of Memphis. After he completes his degree in spring 2021, he plans on going to law school to study patent law. One day, after law school, he hopes to start his own intellectual property law firm. In the summer of 2019, Jacob received a summer research fellowship from the Helen Hardin Honors College. He presented this paper at the Emerging Researchers National Conference in the spring of 2020 in Washington, D.C. When Jacob is not working on physics, he enjoys going to the gym, playing sports, and watching movies.

Jacob Parks

Mars Dust Adhesion: Characterizing Adhesion Behavior
of JSC Mars-1 Regolith on Aerogel Substrates

Faculty Sponsor

Dr. Firouzeh Sabri

Abstract

The adhesion of dust to critical spacecraft equipment poses a major challenge to planetary exploration. Regolith adhesion can cause issues that drastically reduce the length of missions and threaten the safety of astronauts. Regolith adhesion issues have been reported on both lunar and Mars missions, but Mars presents unique challenges due to triboelectrically charged dust suspended in its atmosphere. Mars regolith adhesion has not been studied extensively on aerogels, despite aerogel's rapidly growing number of space applications. The goal of this research was to understand the characteristics and mechanisms of regolith adhesion onto polyimide and polyurea aerogels under different surface charge conditions with Polydimethylsiloxane (PDMS) as a control. Results show that, in general, there is a strong correlation between higher magnitude surface charge and higher regolith accumulation and coverage.

Introduction

The adhesion characteristics of planetary regolith create a significant challenge for planetary exploration. Regolith adhesion, which is caused by Van der Waals and electrostatic forces, can cause major issues on spacecrafts [1]. These issues include reduced solar panel efficiency, damage to mechanical equipment, clogged air filters, and covered calibration targets [2]. These challenges have been reported on both Mars and lunar exploration missions [3]. However, Mars presents unique challenges because Mars' atmosphere contains suspended dust, which has been found to collect on spacecrafts at a rate of 0.28% per day [4]. Additionally, Mars experiences planet-wide dust storms which contribute to triboelectric charging of both Mars dust and spacecrafts, increasing adhesion [5].

One area of regolith adhesion research that is lacking is the characteristics of regolith adhesion onto various types of aerogels. Aerogels are a unique class of materials characterized by their extremely low density, porous structure, low thermal conductivity, and high specific surface area [6]. Because of these properties, aerogels are becoming an attractive material for use in space travel and planetary exploration. Aerogels have already been used in cryogenic fluid containment, thermal insulation on the Mars Rover, and high-velocity particle collection on NASA's *Stardust* [7]. Furthermore, new types of shape-memory aerogels could soon be used as self-deployable structures on spacecrafts [8]. Types of polyimide aerogels have also been considered for use as EDL systems, which will become more important as the size of Mars missions' payloads increase [9]. Thus, understanding dust adhesion to these materials can prevent problems when they are further implemented into planetary exploration. The goal of this research is to understand the mechanisms and causes of the adhesion of JSC Mars-1 simulant regolith onto polyurea-crosslinked and polyimide aerogels under various surface charge conditions, with PDMS as a control.

Experimental Procedures

Surface Potential Measurements

To understand the impact of electrostatic force on the surface of the materials being tested, surface potential measurements were taken using a Kelvin probe. The Kelvin probe used had a vibrating aperture which was 4.5 mm in diameter and was connected to a Trek Model 325 electrostatic voltmeter. Underneath the probe was a stage that allowed for manual x-y-z motion in increments of 1 mm. The probe was placed 1 mm above the sample as is recommended by the manufacturer to avoid fringe fields. Potential Mea-

surements were taken by raster scanning in increments of 1 mm. From the potential readings, charge was calculated for each point using the equation.

$$Q = U \cdot \frac{\epsilon \epsilon_o A}{d}$$

where Q is charge, U is potential, ϵ is the relative electric permittivity of air, ϵ_o is the electric permittivity of vacuum, A is the area of the aperture, and d is the distance between the probe head and the sample.

Regolith Deposition Setup

Regolith deposition experiments were performed in an inverted set up under atmospheric conditions. Each sample was stored in a desiccator to control exposure to humidity prior to regolith deposition. The samples were sonicated in IPA to remove any dust particles on the surface of each sample. The baseline mass and surface charge of each sample was taken using an analytical balance and Kelvin probe, respectively. Samples were then put under one of three surface charge conditions: baseline, neutralized, or charged. These conditions were achieved by using static neutralizing and charging equipment on each sample. The samples in the neutralized condition were discharged using a Takk Ion-Edge model 400T static eliminator bar. The bar was in a fixed position and samples were placed at a distance of 0.5 cm from the bar, as suggested by the manufacturer. For the samples in the charged conditions, samples were first neutralized, then different amounts of charge were deposited onto their surfaces using a Takk 7081 charging bar. Again, the charging bar was fixed 0.5 cm above samples, as suggested by the manufacturer. After the surface charge conditions were placed on each sample, the samples underwent a controlled exposure to the regolith. Using tweezers, each sample was carefully lowered into a petri dish of JSC Mars-1 simulant regolith. The regolith had been treated in a vacuum oven at 105 °C for several days prior to the experiment to remove as much moisture from it as possible. The samples were removed from the regolith carefully so that only the top surface of each sample was exposed to the dust. The samples were shaken three times to remove any large, loose dust particles. The samples were then massed again and analyzed using optical microscopy.
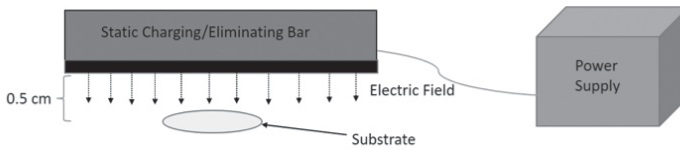
Figure 1. Experimental setup for charging/discharging

ImageJ

The regolith's area coverage on each sample was found from images obtained with a Unitron Examet-5 metallurgical microscope. Percent coverage was calculated through the software ImageJ, which uses thresholding to calculate area coverage. Thresholding is a technique which assigns number values to grayscale images. The software creates a cutoff: any pixel value below the cutoff becomes one category, and any pixel value above the cutoff becomes the other category. The user then must identify which pixel category represents the desired area coverage, and from that percentage the coverage on a substrate can be calculated. Coverage for each substrate was calculated as an average of threshold calculations from several individual images.

Results And Discussion

Surface Potential

Baseline surface potential measurements showed a wide range of potential on each substrate. The results of these measurements are shown in Figure 2. Both the polyurea aerogel and the JSC Mars-1 simulant regolith itself were found to have a weak positive surface potential, and, therefore, weak surface charge. Polyimide aerogels and PDMS both exhibited a high magnitude negative surface potential and charge.
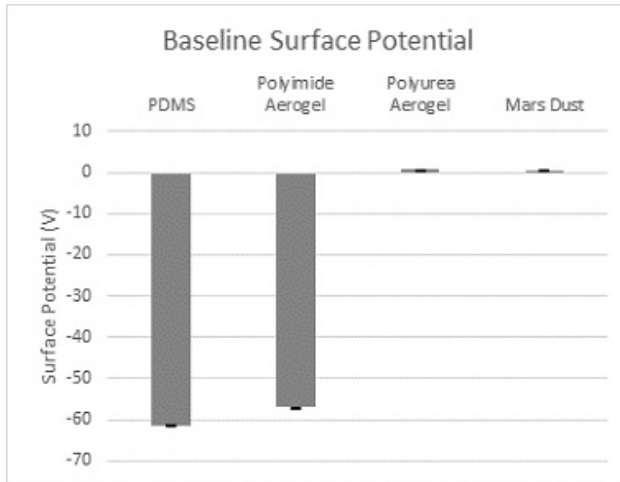
Figure 2. Average baseline surface potential for PDMS, polyimide aerogel, polyurea aerogel, and the Mars regolith.

Furthermore, the PDMS and polyimide aerogels exhibited a more uniform potential distribution over the surface, shown in Figures 3a and 3b, respectively. The polyurea aerogel showed a more varied surface potential, with areas of higher and lower relative potential throughout the scanned area, as shown in Figure 3c.
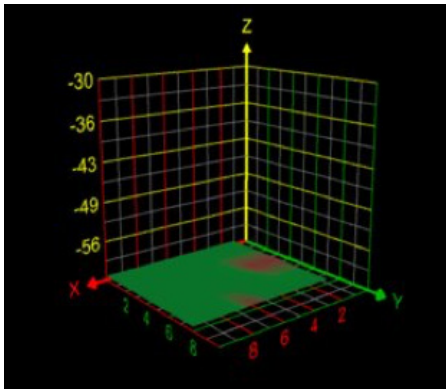
(a)
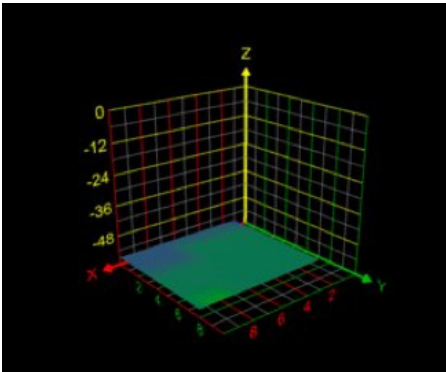
(b)
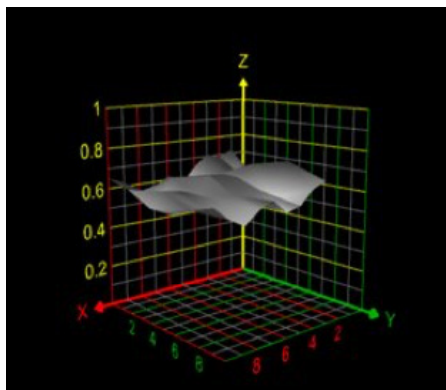
(c)

Figure 3. Surface Potential Distribution for (a) PDMS (b) polyimide aerogel and (c) polyurea aerogel. The z-axis represents the surface potential in volts.

After electrostatic charging, the change in surface potential after neutralization was found for applied voltages from 1 to 10 kV. Each substrate exhibited similar properties when undergoing changes to surface charge. The samples experienced incrementally higher changes in surface potential with each step of applied voltage until a dielectric limit was reached, as shown in Figure 4. This dielectric limit occurred at 5 kV for PDMS, 6 kV for the polyimide aerogel, and 7kV for the polyurea aerogel. After this limit was reached, no more surface potential could be added to the surface, even with higher applied voltages.
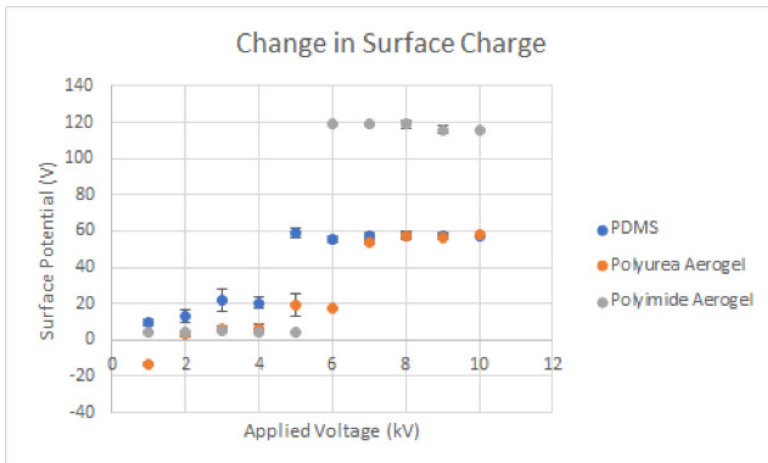

Figure 4. Change in surface charge for PDMS, Polyurea aerogels, and polyimide aerogels.

Gravimetric Analysis

After the dust was deposited onto each substrate using the inverted method, the masses were taken and compared to the baseline for each sample. The results of the gravimetric analysis of the samples at baseline surface charge are shown in Figure 5. At baseline surface charge, PDMS had the highest regolith accumulation, followed by the polyimide aerogel. The polyurea aerogel had the lowest accumulation (Fig. 5). This suggests that the higher the magnitude of surface charge, the higher the regolith accumulation. The regolith accumulation on the samples with 10, 15, and 20 kV of applied potential is also shown in Figure 5. For each sample, except for polyimide aerogel, the regolith accumulation was higher on the charged surfaces than the baseline samples. This is because applying voltage increases the surface potential, thus increasing accumulation.
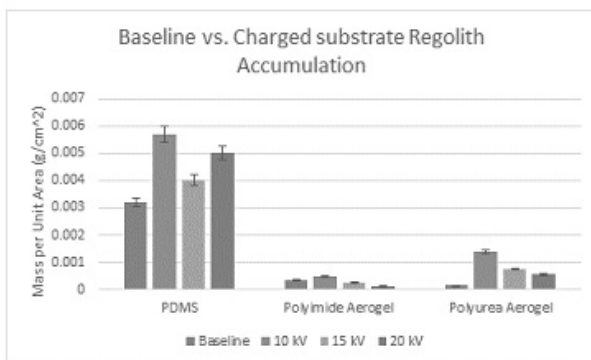
Figure 5. Regolith accumulation for each substrate at baseline, 10 kV, 15 kV, and 20 kV.

For each sample, the highest accumulation occurred at 10 kV. This is a direct result of the dielectric limit of each material being below 10 kV. For applied voltages higher than 10 kV, no additional surface potential was being added, so there was no additional regolith accumulation. The results shown in Figure 5 also suggest that the charge of the sample induces an opposite charge on the Mars regolith. Figure 2 shows that at baseline, Mars regolith has a weak positive surface potential. PDMS and polyimide aerogels at baseline have high negative surface potential, while polyurea aerogels have weak positive surface potential at baseline. PDMS and polyimide aerogels both exhibited a change in polarity with high applied voltages. This shows that the Mars regolith can take on both positive and negative charge, because there was adhesion to each substrate regardless of its surface charge polarity. The results of the gravimetric analysis of the neutralized samples are shown in Figure 6. For each neutralized sample, regolith accumulation was lower when compared to the baseline.
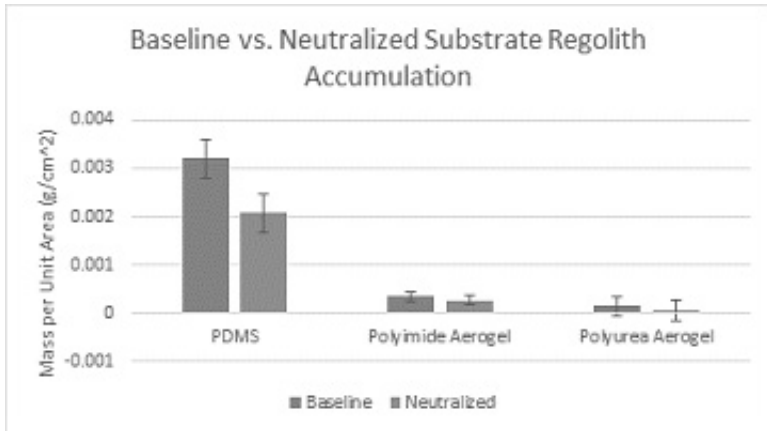
Figure 6. Regolith accumulation for each substrate at baseline and after neutralization.

These results again show that higher magnitude surface potential leads to higher regolith accumulation. This also confirms that other factors influence adhesion, because even with the low magnitude surface potential after neutralization, each substrate still accumulated regolith.

Optical Microscopy

The percentage of the substrate area covered by Mars regolith was calculated for each sample using ImageJ software. From this data, a clear relationship between higher surface charge and a higher concentration of dust adhering to the surface of each substrate can be seen. PDMS and polyimide aerogels exhibited the highest and most uniform coverage. The polyurea crosslinked aerogel, which had lower and less uniform charge, exhibited lower and less uniform coverage.
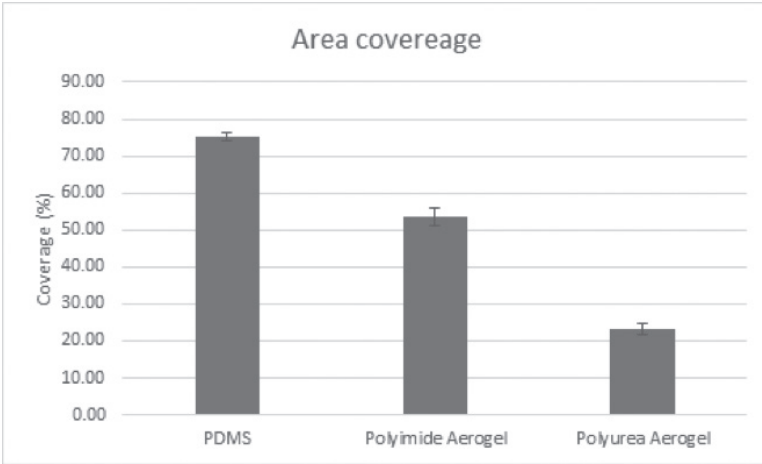
Figure 7. Areal coverage for each substrate at baseline surface potential.

The regolith coverage for the other surface potential conditions still needs to be explored. Another observation from optical microscope images was a towering effect which occurred on each substrate. The Mars regolith showed dust-dust adhesion as particles adhered to one another and stacked vertically on the substrate, as described by the schematic in Figure 8. Again, this shows evidence that the polarity of the Martian regolith can be influenced by the surface of the substrate as well as other regolith particles.
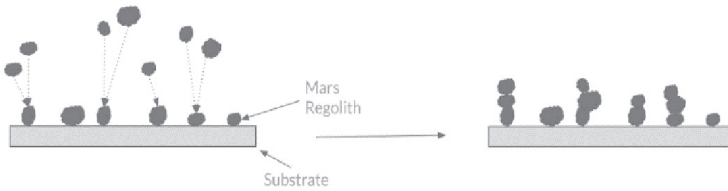

Figure 8. Schematic describing the towering effect

Conclusion

Adhesion characteristics of JSC Mars-1 simulant dust were explored through experimental methods. Experiments were performed on samples with a variety of surface charge conditions under atmospheric conditions in an inverted experimental setup. The effects of surface charge on adhesion behavior was very clear. Higher surface charge on PDMS and polyimide aerogels led to higher area coverage and more regolith adhesion by mass. Lower surface charge, consequently, led to lower coverage and regolith adhesion by mass. When voltage is applied onto the surface of a substrate, a dielectric limit is reached and surface potential no longer increases. This, in turn, keeps regolith adhesion from increasing infinitely as supplied voltage gets higher. Another characteristic of adhesion seen was the towering effect, which shows that there is dust-dust adhesion as well as adhesion between the dust and the substrate itself. This also shows that the samples and other regolith particles can change and induce charge in the Mars Regolith. Further exploration into the effects of low pressure, low humidity, different applied voltages, and temperature will need to be explored using the inverted experimental setup. Surface roughness measurements will also need to be taken before and after dust exposure to explore the relationship between adhesion behavior and surface roughness.

References

[1] F. Sabri, T. Werhner, J. Hoskins, A. Schuerger, A. Hobbs, J. Barreto, D. Britt, and R. Duran, Advances in Space Research **41**, 118 (2008).

[2] H. Perko, J. Nelson, and J. Green, Proceedings of Engineering, Infrastructure, and Sciences, 1 (2002).

[3] T. Stubbs, R. Vondrak, and W. Farrell in: *Dust in Planetary Systems*, (NASA, Kauai, HI, 2005, pp. 239-243).

[4] G. Landis and P. Jenkins, Journal of Geophysical Research 105, 1855 (2000).

[5] Z. Sternovsky, S. Robertson, A. Sickafoose, J. Colwell, and M. Horanyi, Journal of Geophysical Research **107**, 15 (2002).

[6] A. Pierre and G. Pajonk, Chem. Rev. **102**, 4243 (2002).

[7] S. Jones, J Sol-Gel Sci Techn **40**, 351 (2006).

[8] W. Sokolowski and S. Tan, Journal of Spacecraft and Rockets, 1 (2007).

[9] M. Meador, E. Malow, R. Silva, S. Wright, D. Quade, S. Vivod, H. Guo, J. Guo, and M. Cakmak, ACS Appl. Mater. Interfaces, **4(2)**, 536 (2012).